

# A combined analysis of short-baseline neutrino experiments in the (3+1) and (3+2) sterile neutrino oscillation hypotheses

M. Sorel,<sup>\*</sup> J. M. Conrad,<sup>†</sup> and M. H. Shaevitz<sup>‡</sup>  
*Department of Physics, Columbia University, New York, NY 10027*  
 (Dated: May 12, 2019)

We investigate adding two sterile neutrinos to resolve the apparent tension existing between short-baseline neutrino oscillation results and CPT-conserving, four-neutrino oscillation models. For both (3+1) and (3+2) models, the level of statistical compatibility between the combined dataset from the null short-baseline experiments Bugey, CHOOZ, CCFR84, CDHS, KARMEN, and NOMAD, on the one hand; and the LSND dataset, on the other, is computed. A combined analysis of all seven short-baseline experiments, including LSND, is also performed, to obtain the favored regions in neutrino mass and mixing parameter space for both models. Finally, four statistical tests to compare the (3+1) and the (3+2) hypotheses are discussed. All tests show that (3+2) models fit the existing short-baseline data significantly better than (3+1) models.

PACS numbers: 14.60.Pq, 14.60.St, 12.15.Ff

## I. INTRODUCTION

There currently exist three experimental signatures for neutrino oscillations. The two signatures seen originally in solar and atmospheric neutrinos have been verified by several experiments, including experiments carried out with accelerator and nuclear reactor sources. The results on atmospheric neutrinos can be explained by  $\nu_\mu$  disappearance due to oscillations [1, 2, 3], while those on solar neutrinos can be explained by  $\nu_e$  oscillations [4, 5]. The third signature is  $\bar{\nu}_e$  appearance in a  $\bar{\nu}_\mu$  beam, observed by the short-baseline, accelerator-based LSND experiment at Los Alamos [6]. This signature is strong from a statistical point of view, being a  $3.8\sigma$  excess, but further confirmation by an independent experiment is necessary. The MiniBooNE experiment at Fermilab will be able to confirm or refute the LSND signature in the near future, with an experimental setup providing different systematics and higher statistics than LSND [7].

Taken at face value, the three experimental signatures point to three independent mass splittings. Three neutrino masses do not appear to be able to explain all of the three signatures [8, 9] (see, however, [10]). One way to solve this puzzle is to introduce different mass spectra for the neutrino and antineutrino sector, thereby requiring CPT-violation but no extra neutrino generations [11]. Another possibility is to add additional neutrinos with no standard weak couplings, often called “sterile neutrinos”.

In this paper we assume CPT- and CP-invariance, and we explore the possibility of adding one or two neutrino generations beyond the three active flavors assumed by the Standard Model. We focus on extensions of the neutrino sector where the addition of fourth and fifth mass eigenstates are responsible for the high  $\Delta m^2$  LSND oscil-

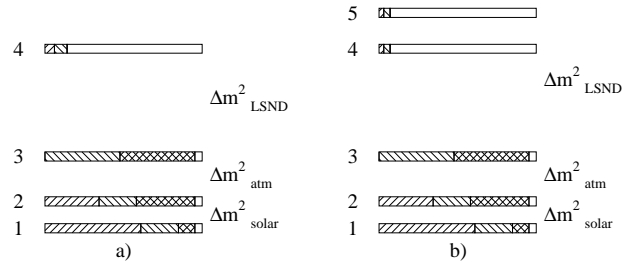


FIG. 1: Flavor content of neutrino mass eigenstates in (3+1) models (a), and (3+2) models (b). Neutrino masses increase from bottom to top. The  $\nu_e$  fractions are indicated by right-leaning hatches, the  $\nu_\mu$  fractions by left-leaning hatches, the  $\nu_\tau$  fractions by crosshatches, and the  $\nu_s$  fractions by no hatches. The flavor contents shown are schematic only.

lations, and the three lower mass states explain solar and atmospheric oscillations. When only one sterile neutrino is added, these models are labelled as (3+1). The flavor content of the four neutrino mass eigenstates for these models is schematically shown in Fig. 1a. The (3+1) hierarchy in Fig. 1a is as opposed to the (2+2) hierarchy, where the solar and atmospheric mass splittings are separated from each other by the LSND  $\Delta m^2$ . The (2+2) models require a different global analysis from the one discussed in this paper. The simplest (2+2) models appear to be only marginally consistent with neutrino oscillations data [8, 12], even though more general (2+2) mass and mixing scenarios might represent a viable solution to explain solar, atmospheric, and LSND oscillations [13].

The (3+1) models are motivated by the criterion of simplicity in physics, introducing the most minimal extension to the Standard Model that explains the experimental evidence. However, theories invoking sterile neutrinos to explain the origin of neutrino masses do not necessarily require only one sterile neutrino. Indeed, many popular realizations of the see-saw mechanism in-

<sup>\*</sup>Electronic address: sorel@nevis.columbia.edu

<sup>†</sup>Electronic address: conrad@nevis.columbia.edu

<sup>‡</sup>Electronic address: shaevitz@nevis.columbia.edu

roduce three right-handed neutrino fields [14, 15, 16]. In particular, (3+2) neutrino mass and mixing models can be obtained in several see-saw mechanisms [17]. From the phenomenological point of view, it is our opinion that two- and three-sterile neutrino models should also be considered and confronted with existing experimental results. In this paper, we consider the results from the short-baseline experiments Bugey [18], CCFR84 [19], CDHS [20], CHOOZ [21], KARMEN [22], LSND [6], and NOMAD [23], and examine how well (3+1) and (3+2) models agree with data. A schematic diagram for (3+2) models is shown in Fig. 1b. We do not consider (3+3) models in this paper. From our initial studies, we believe that the phenomenology of a (3+3) model is similar to a (3+2) model.

The paper is organized as follows. In Section II, we specify the neutrino oscillations formalism used in this analysis to describe (3+1) and (3+2), short-baseline, oscillations. In Section III and IV, we present the results obtained for the (3+1) and (3+2) models, respectively. For both models, we first derive the level of compatibility between the null short-baseline (NSBL) experiments and LSND. Second, we perform a combined analysis of all seven short-baseline experiments (including LSND) to derive the preferred regions in neutrino mass and mixing parameter space. In Section V, we discuss four statistical tests to compare the (3+1) and (3+2) hypotheses. In Section VI, we briefly mention other experimental constraints on (3+1) and (3+2) models. In Appendix A, we describe the physics and statistical assumptions used in the analysis to describe the short-baseline experiments.

## II. NEUTRINO OSCILLATIONS FORMALISM

Under the assumptions of CP- and CPT-invariance, the probability for a neutrino, produced with flavor  $\alpha$  and energy  $E$ , to be detected as a neutrino of flavor  $\beta$  after travelling a distance  $L$ , is [24]:

$$P(\nu_\alpha \rightarrow \nu_\beta) = \delta_{\alpha\beta} - 4 \sum_{j>i}^n U_{\alpha,j} U_{\beta,j} U_{\alpha,i} U_{\beta,i} \sin^2 x_{ji} \quad (1)$$

where  $\alpha = e, \mu, \tau, s$  ( $s$  being the sterile flavor);  $U$  is the unitary neutrino mixing matrix;  $x_{ji} \equiv 1.27 \Delta m_{ji}^2 L/E$ ;  $\Delta m_{ji}^2 \equiv m_j^2 - m_i^2$ ; and  $n$  is the number of neutrino generations. Neglecting CP-violating phases, there are in general  $(n-1)$  independent mass splittings, and  $n^2 - n - n(n-1)/2$  independent mixing matrix elements. The situation simplifies considerably by considering short-baseline (SBL) data only. In this case, it is a

good approximation to assume  $x_{21} = x_{32} = 0$ , and only  $(n-3)$  independent mass splittings are present. Moreover, given the set of SBL experiments considered, the number of mixing matrix elements probed is only  $2(n-3)$ , as we show now for the (3+1) and (3+2) cases.

For (3+1) models,  $n=4$ , and only one mass splitting  $\Delta m^2 \equiv \Delta m_{41}^2 \simeq \Delta m_{42}^2 \simeq \Delta m_{43}^2$  appears in the oscillation formula: this is sometimes referred to as the “quasi-two-neutrino approximation”, or “one mass scale dominance” [25]. Using the unitarity properties of the mixing matrix, we can rewrite Eq. 1 for (3+1) models in a more convenient way:

$$P(\nu_\alpha \rightarrow \nu_\beta) = \delta_{\alpha\beta} - 4U_{\alpha 4}U_{\beta 4}(\delta_{\alpha\beta} - U_{\alpha 4}U_{\beta 4})\sin^2 x_{41} \quad (2)$$

which depends on the mass splitting ( $\Delta m_{41}^2$ ) and mixing parameters ( $U_{\alpha 4}$ ,  $U_{\beta 4}$ ) of the fourth generation only. Since the two-neutrino approximation is satisfied in the (3+1) case, we can express Eq. 2 in the usual forms:

$$P(\nu_\alpha \rightarrow \nu_\beta) = \sin^2 2\theta_{\alpha\beta} \sin^2 x_{41}, \quad \alpha \neq \beta \quad (3)$$

$$P(\nu_\alpha \rightarrow \nu_\alpha) = 1 - \sin^2 2\theta_{\alpha\alpha} \sin^2 x_{41} \quad (4)$$

where Eq. 3 applies to an oscillation appearance measurement, Eq. 4 to a disappearance measurement.

In this paper, we use the data from the Bugey, CCFR84, CDHS, CHOOZ, KARMEN, LSND, and NOMAD experiments. Bugey and CHOOZ data constrain  $\bar{\nu}_e$  disappearance; CCFR84 and CDHS data constrain  $\nu_\mu$  disappearance; and KARMEN, LSND, and NOMAD data constrain  $\bar{\nu}_\mu \rightarrow \bar{\nu}_e$  oscillations. Therefore, from Eqs. 2,3, and 4, the experiments constrain the following combinations of (3+1) mixing parameters:

- Bugey, CHOOZ:  $\sin^2 2\theta_{ee} \equiv 4U_{e4}^2(1 - U_{e4}^2)$ ;
- CCFR84, CDHS:  $\sin^2 2\theta_{\mu\mu} \equiv 4U_{\mu 4}^2(1 - U_{\mu 4}^2)$ ;
- KARMEN, LSND, NOMAD:  $\sin^2 2\theta_{\mu e} \equiv 4U_{e4}^2 U_{\mu 4}^2$ .

In (3+1) models, the tension between the experimental results comes about because Bugey, CHOOZ, CCFR84, CDHS, KARMEN, and NOMAD limit the two independent mixing matrix parameters  $U_{e4}$  and  $U_{\mu 4}$  to be small, whereas LSND demands nonzero values.

In (3+2) models, we introduce two sterile neutrinos. Using Eq. 1 and the unitarity of the mixing matrix, the (3+2) neutrino oscillation probability formula can be written:

$$\begin{aligned} P(\nu_\alpha \rightarrow \nu_\beta) &= \delta_{\alpha\beta} - 4[(\delta_{\alpha\beta} - U_{\alpha 4}U_{\beta 4} - U_{\alpha 5}U_{\beta 5})(U_{\alpha 4}U_{\beta 4} \sin^2 x_{41} + U_{\alpha 5}U_{\beta 5} \sin^2 x_{51}) + U_{\alpha 4}U_{\alpha 5}U_{\beta 4}U_{\beta 5} \sin^2 x_{54}] = \\ &= \delta_{\alpha\beta} + 4[U_{\alpha 4}^2(U_{\beta 4}^2 - \delta_{\alpha\beta}) \sin^2 x_{41} + U_{\alpha 5}^2(U_{\beta 5}^2 - \delta_{\alpha\beta}) \sin^2 x_{51} + U_{\alpha 4}U_{\beta 4}U_{\alpha 5}U_{\beta 5}(\sin^2 x_{41} + \sin^2 x_{51} - \sin^2 x_{54})] \quad (5) \end{aligned}$$

which in our case depends on two independent mass splittings ( $\Delta m_{41}^2, \Delta m_{51}^2$ ) and four independent mixing matrix parameters ( $U_{\alpha 4}, U_{\alpha 5}$ , with  $\alpha = e, \mu$ ). Eq. 2 can be recovered from Eq. 5 by requiring  $U_{\alpha 5} = U_{\beta 5} = 0$ . In (3+2) models, the quasi-two-neutrino-approximation is not valid, since there are three distinct  $\Delta m^2$  values contributing in the oscillation formula:  $\Delta m_{41}^2$ ,  $\Delta m_{51}^2$ , and  $\Delta m_{54}^2$ , and therefore three distinct oscillation amplitudes:  $(\sin^2 2\theta_{\alpha\beta})_{41}$ ,  $(\sin^2 2\theta_{\alpha\beta})_{51}$ , and  $(\sin^2 2\theta_{\alpha\beta})_{54}$ .

We now comment on the Monte Carlo method used to apply the above oscillation formalism to the analyses presented in this paper. We require the neutrino mass splittings to be in the range  $0.1 \text{ eV}^2 \leq \Delta m_{41}^2, \Delta m_{51}^2 \leq 100 \text{ eV}^2$ , with  $\Delta m_{51}^2 \geq \Delta m_{41}^2$ . Each mass splitting range is analyzed over a 200 point grid, uniformly in  $\log_{10} \Delta m^2$ . In Section VI, we briefly discuss why large mass splittings are not necessarily in contradiction with cosmological (and other) data. The values of the mixing parameters,  $U_{e4}, U_{\mu 4}, U_{e5}$ , and  $U_{\mu 5}$ , are randomly generated over a four-dimensional space satisfying the four requirements:  $U_{ei}^2 + U_{\mu i}^2 \leq 0.5$ ,  $U_{\alpha 4}^2 + U_{\alpha 5}^2 \leq 0.5$ , where:  $i = 4, 5$ ,  $\alpha = e, \mu$ . These four inequalities are introduced to account for the fact that large electron and muon flavor fractions in the fourth and fifth mass eigenstates are not allowed by solar and atmospheric neutrino data. In principle, since the CDHS constraint on  $\nu_\mu$  disappearance vanishes for  $\Delta m^2 \simeq 0.3 \text{ eV}^2$ , as shown in Appendix A, the upper limit on  $\nu_\mu$  disappearance from atmospheric neutrino experiments above the atmospheric  $\Delta m^2$  should be considered instead. In this paper, we do not reconstruct the likelihood for atmospheric data that would give the exclusion region for  $\nu_\mu$  disappearance in the range  $\Delta m_{atm}^2 \ll \Delta m^2 < 0.3 \text{ eV}^2$ . However, the effect that the atmospheric constraints would have on our results is expected to be small. For example, in Ref. [33], Bilenyk *et al.* use the atmospheric up-down asymmetry to derive the upper limit  $U_{\mu 4}^2 < 0.55$  at 90% CL for (3+1) models, which is satisfied by our initial requirements  $U_{e4}^2 + U_{\mu 4}^2 < 0.5$ ,  $U_{\mu 4}^2 + U_{\mu 5}^2 < 0.5$ . A more recent analysis [34] of atmospheric neutrino data using the full zenith angle distribution provides a tighter constraint on  $\sin^2 \theta_{\mu\mu}$  than the one given in Ref. [33]; the impact of this additional constraint on our SBL analysis is discussed in Sections III and VI. Finally, from Eqs. 2, it is clear that the relative sign of both  $U_{e4}$  and  $U_{\mu 4}$  cannot be inferred in (3+1) oscillations. Similarly, from Eq. 5, the only physically observable relative sign between mixing parameters in CP-conserving (3+2) models is  $sign(U_{e4}U_{\mu 4}U_{e5}U_{\mu 5})$ ; therefore, this is the only sign related to mixing parameters that we randomly generate in the analysis.

Throughout the paper, we make use of the Gaussian approximation in determining allowed regions in parameter space. In general, this means that the regions of quoted confidence level are the ones enclosed by contours of constant  $\chi^2$  values, whose differences with respect to the best-fit  $\chi^2$  value depend on the number

of free parameters in the model [31]. In the text, we use the symbol  $\delta$  to denote the values of the confidence levels derived in this way. As pointed out in [32], this approach should be considered approximate, as it may provide regions in parameter space of both higher and lower confidence than the one quoted. Regions of higher confidence than the quoted value may result from the presence of highly correlated parameters. Regions of lower confidence may result from the presence of fast oscillatory behavior of the oscillation probability formula, Eq. 1.

### III. RESULTS FOR (3+1) MODELS

This section, like the next one on (3+2) models, consists of two parts. First, we quantify the statistical compatibility between the NSBL and LSND results, following a method described in [26, 27], originally proposed to establish the compatibility between the LSND and KARMEN results. Second, we perform a combined analysis of the NSBL and LSND datasets, to obtain the favored regions in neutrino mass and mixing parameter space.

#### A. Statistical compatibility between NSBL and LSND

Many analyses of the NSBL experiments within (3+1) models have concluded that the allowed LSND region is largely excluded [28, 29, 30]. Here, we repeat this study with two purposes. First, we use this study to give context to our discussion of the basic model and techniques which will be expanded in later sections. Second, we demonstrate that our fit, which forms the basis of our new results for (3+2) models, reproduces the expected (3+1) exclusion region. For a discussion of the physics and statistical assumptions used to describe the short-baseline experiments used in the analysis, the reader should refer to Appendix A.

In this section, the NSBL and LSND datasets are analyzed separately, providing two independent allowed regions in  $(\sin^2 2\theta_{\mu e}, \Delta m^2)$  space. The level of statistical compatibility between the two datasets can be determined by studying to what degree the two allowed regions overlap, as will be quantified later in this section.

For each randomly generated (3+1) model, we calculate the values for the  $\chi^2$  functions  $\chi_{\text{NSBL}}^2$  and  $\chi_{\text{LSND}}^2$ , where  $\chi_{\text{NSBL}}^2$  is defined as:

$$\chi_{\text{NSBL}}^2 \equiv \chi_{\text{Bugey}}^2 + \chi_{\text{CHOOZ}}^2 + \chi_{\text{CCFR84}}^2 + \chi_{\text{CDHS}}^2 + \chi_{\text{KARMEN}}^2 + \chi_{\text{NOMAD}}^2 \quad (6)$$

For the analysis described in this section, the NSBL and LSND allowed regions are obtained using two different algorithms, reflecting the fact that the NSBL dataset provides upper limits on oscillations, while the LSND dataset points to non-null oscillations.

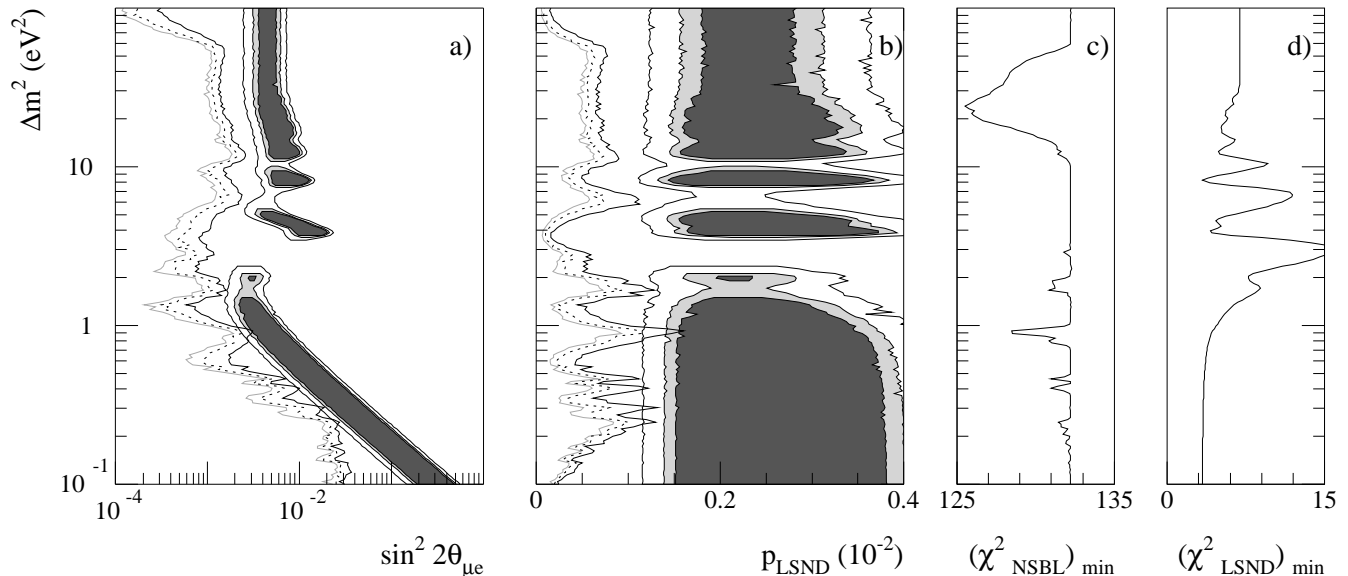


FIG. 2: Compatibility between the NSBL and LSND datasets in (3+1) models. Fig. 2a shows the 90% (grey solid line), 95% (black dotted line), and 99% (black solid line) CL exclusion curves in  $(\sin^2 2\theta_{\mu e}, \Delta m^2)$  space for (3+1) models, considering the null short-baseline (NSBL) experiments Bugey, CCFR84, CDHS, CHOOZ, KARMEN, and NOMAD. Fig. 2a also shows the 90%, 95%, and 99% CL allowed regions by our analysis of LSND data. Fig. 2b) is as Fig. 2a, but in  $(p_{\text{LSND}}, \Delta m^2)$  space, where  $p_{\text{LSND}}$  is the LSND oscillation probability (see text for the definition). Fig. 2c) and d) show the minimum  $\chi^2$  values as a function of  $\Delta m^2$  for the NSBL and LSND datasets (143 and 3 d.o.f., respectively).

The NSBL allowed regions at various confidence levels  $\delta_{\text{NSBL}}$  are obtained via a raster scan algorithm [32]. Let  $\chi_{\text{NSBL}}^2$  be the  $\chi^2$  value for the particular model and  $(\chi_{\text{NSBL}}^2)_{\text{min}, \Delta m^2}$  be the minimum  $\chi^2$  for the  $\Delta m^2$  value considered. For example, our quoted 95% CL upper limit on  $\sin^2 2\theta_{\mu e}$  is given by the maximum value for the product  $4U_{e4}^2 U_{\mu 4}^2$  chosen among the models which satisfy the inequality  $\chi_{\text{NSBL}}^2 - (\chi_{\text{NSBL}}^2)_{\text{min}, \Delta m^2} < 5.99$ . The value of 5.99 units of  $\chi^2$  is chosen because there are two free parameters  $U_{e4}$ ,  $U_{\mu 4}$  for (3+1) models with fixed  $\Delta m^2$ . We note that even for the NSBL dataset, the parameters  $U_{e4}$ ,  $U_{\mu 4}$  can be correlated, since the KARMEN and NOMAD results probe a combination of the two parameters.

The LSND allowed regions at various confidence levels  $\delta_{\text{LSND}}$  are obtained via a global scan algorithm [32]. For example, for  $\delta_{\text{LSND}} = 0.95$  we require  $\chi_{\text{LSND}}^2 - (\chi_{\text{LSND}}^2)_{\text{min}} < 5.99$ , where  $(\chi_{\text{LSND}}^2)_{\text{min}}$  is now the global LSND  $\chi^2$  minimum value, considering all possible  $\Delta m^2$  values. The LSND allowed region is computed for two free parameters as for the NSBL case, but the parameters are now  $\Delta m^2$  and  $U_{\mu 4} U_{e4}$ , as opposed to  $U_{\mu 4}$  and  $U_{e4}$ . Compared to the NSBL case, the number of free parameters is reduced by one because the LSND  $\bar{\nu}_\mu \rightarrow \bar{\nu}_e$  search only probes the product  $U_{\mu 4} U_{e4}$  and not the two mixing matrix elements individually, and it is increased by one because the allowed region is now obtained by scanning over all possible  $\Delta m^2$  values.

The regions allowed in  $(\sin^2 2\theta_{\mu e}, \Delta m^2)$  parameter space by both the NSBL and LSND datasets are shown in Fig. 2a. The NSBL allowed regions shown are 2-

dimensional projections of 3-dimensional allowed regions in  $(\Delta m^2, U_{e4}, U_{\mu 4})$  space. The NSBL results alone allow the regions to the left of the solid grey, dotted black, and solid black lines in the Fig. 2a, at a confidence level  $\delta_{\text{NSBL}} = 0.90, 0.95, 0.99$ , respectively. In Fig. 2a, the  $\delta_{\text{LSND}} = 0.90, 0.95, 0.99$  CL allowed regions obtained by our analysis for LSND data are also shown, as dark grey shaded, light grey shaded, and white areas, respectively. We find no overlap between the two individual 95% CL allowed regions; on the other hand, there is overlap between the two 99% CL regions.

Fig. 2b shows the same (3+1) allowed regions as Fig. 2a but in the  $(p_{\text{LSND}}, \Delta m^2)$  plane, where  $p_{\text{LSND}}$  is defined as the  $\nu_\mu \rightarrow \nu_e$  oscillation probability averaged over the LSND  $L/E$  distribution:

$$p_{\text{LSND}} \equiv \langle P(\nu_\mu \rightarrow \nu_e) \rangle \quad (7)$$

where  $P(\nu_\mu \rightarrow \nu_e)$  is given by Eq. 1 for  $\alpha = \mu$ ,  $\beta = e$ , and is a function of all the mass and mixing parameters of the oscillation model under consideration. This has the obvious disadvantage of being a quantity dependent upon the specifics of a certain experiment, as opposed to a universal variable such as  $\sin^2 2\theta_{\mu e} = 4U_{\mu 4}^2 U_{e4}^2$ . However,  $p_{\text{LSND}}$  has the advantage of being unambiguously defined for any number of neutrino generations, and thus is useful in discussing (3+2) models later in this paper. As stated previously, the oscillation probability estimator  $\sin^2 2\theta_{\mu e} = 4U_{\mu 4}^2 U_{e4}^2$  cannot be used when more than one  $\Delta m^2$  value affects the oscillation probability, as is the case for (3+2) models. A second advantage of using  $p_{\text{LSND}}$

instead of  $\sin^2 2\theta_{\mu e}$  as the oscillation probability estimator, is that the allowed values for  $p_{\text{LSND}}$  inferred from the LSND result tend to be almost  $\Delta m^2$ -independent (see grey-shaded areas in Fig. 2b), as expected for an almost pure counting experiment such as LSND. The oscillation probability reported by the LSND collaboration [6] is  $p_{\text{LSND}} = (0.264 \pm 0.067 \pm 0.045)\%$ , and agrees well with our result of Fig. 2b.

Fig. 2c shows the values for  $(\chi_{\text{NSBL}}^2)_{\text{min}}$  as a function of  $\Delta m^2$ . The number of degrees of freedom is 143. As discussed in Appendix A, the dip in  $(\chi_{\text{NSBL}}^2)_{\text{min}}$  at  $\Delta m^2 \simeq 0.9 \text{ eV}^2$  is due to Bugey data preferring  $U_{e4} \neq 0$  values, while the minimum at  $\Delta m^2 \sim 10 - 30 \text{ eV}^2$  is due to CDHS (mostly) and CCFR84 data, preferring  $U_{\mu 4} \neq 0$  values. The  $\chi^2$  value for no oscillations,  $(\chi_{\text{NSBL}}^2)_{\text{no osc}} = 132.2$ , is the largest  $\chi^2$  value in Fig. 2c; this means that the choice of parameters  $U_{e4} = U_{\mu 4} = 0$  provides the best-fit to NSBL data, for the  $\Delta m^2$  values satisfying the condition  $(\chi_{\text{NSBL}}^2)_{\text{min}} = (\chi_{\text{NSBL}}^2)_{\text{no osc}}$ . Note that the  $\Delta m^2 \simeq 0.9 \text{ eV}^2$ ,  $\Delta m^2 \simeq 10 - 30 \text{ eV}^2$  dips in  $\chi_{\text{NSBL}}^2$  are consistent with  $U_{e4}U_{\mu 4} = 0$ , and therefore with  $\sin^2 2\theta_{\mu e} = p_{\text{LSND}} = 0$ , but give better fits than the no-oscillations hypothesis,  $U_{e4} = U_{\mu 4} = 0$ . In other words, the goodness of fit for the  $\sin^2 2\theta_{\mu e} = p_{\text{LSND}} = 0$  region depends on the  $\Delta m^2$  value considered.

Similarly, Fig. 2d shows the values for  $(\chi_{\text{LSND}}^2)_{\text{min}}$  as a function of  $\Delta m^2$ , used to obtain the LSND allowed regions drawn in Figs. 2a, 2b.

We now present a slightly different approach to determine the statistical compatibility between the NSBL and LSND datasets in (3+1) models, which will prove useful in comparing the (3+1) and (3+2) hypotheses.

In Fig. 3, we show the values for the  $\chi^2$  differences  $\Delta\chi_{\text{NSBL}}^2$ ,  $\Delta\chi_{\text{LSND}}^2$ , as well as the corresponding confidence levels  $\delta_{\text{NSBL}}$ ,  $\delta_{\text{LSND}}$ , as a function of the LSND oscillation probability. The curves are for the set of (3+1) models with the neutrino mass splitting  $\Delta m^2$  fixed to the best-fit value obtained in a combined NSBL+LSND analysis (see Section III B),  $\Delta m^2 = 0.92 \text{ eV}^2$ , and mixing matrix elements  $U_{\mu 4}$ ,  $U_{e4}$  treated as free parameters. The value for  $\Delta m^2$  is chosen in this way because it represents to a good approximation the value for which one expects the best compatibility between the two datasets, as can also be seen in Fig. 2b. In Fig. 3a, we map the  $(U_{e4}, U_{\mu 4})$  allowed space into an the  $(p_{\text{LSND}}, \chi_{\text{NSBL}}^2)$ ,  $(p_{\text{LSND}}, \chi_{\text{LSND}}^2)$  spaces. For any given value of  $p_{\text{LSND}}$ , the minima for the  $\chi_{\text{NSBL}}^2$  and  $\chi_{\text{LSND}}^2$  functions are found in the two  $(U_{e4}, U_{\mu 4})$  and one  $(U_{e4}U_{\mu 4})$  free parameters available, respectively. The process is repeated for several  $p_{\text{LSND}}$  values, and the collection of these minima for all values of  $p_{\text{LSND}}$  give the two curves in Fig. 3a. The individual confidence levels  $\delta_{\text{NSBL}}$ ,  $\delta_{\text{LSND}}$ , shown in Fig. 3b, are obtained from  $\Delta\chi_{\text{NSBL}}^2$ ,  $\Delta\chi_{\text{LSND}}^2$  in the usual way, by assuming one and two free parameters for the LSND and NSBL datasets, respectively.

We now address how to extract areas in parameter space of a given combined confidence  $\delta$  from two independent experimental constraints, in our case obtained via

the NSBL and LSND datasets, without assuming statistical compatibility *a priori*. The most straightforward way (described, for example, in [26, 27]) is to assign a confidence level  $\delta = \delta_{\text{NSBL}}(\delta_{\text{LSND}} + (1 - \delta_{\text{LSND}})/2)$  to the overlapping part (if any) between the two separate allowed regions in parameter space which are found with the constraint  $\delta_{\text{NSBL}} = \delta_{\text{LSND}}$ . The extra factor  $(1 - \delta_{\text{LSND}})/2$  is due to the fact that the LSND allowed region in the oscillation probability is two-sided, and overlap with the NSBL result on the same probability is obtained only for downward fluctuations in the LSND result, and not for upward ones.

From Fig. 3b, we find overlapping allowed ranges in  $p_{\text{LSND}}$  for  $1 - \delta_{\text{NSBL}} = 1 - \delta_{\text{LSND}} \simeq 2.4\%$ . We conclude that, in (3+1) models, the LSND and NSBL datasets are incompatible at a combined confidence of  $\delta \simeq 96.4\%$ . In our opinion, this value does not support any conclusive statements against the statistical compatibility between NSBL and LSND data in (3+1) models, although it represents poor agreement between the two datasets. The reader should also refer to Section V D, where a different method to quantify the compatibility between the NSBL and LSND results is discussed. Future short-baseline constraints on  $\nu_{\mu} \rightarrow \nu_e$  appearance, as well as on  $\nu_{\mu}$  and  $\nu_e$  disappearance, should be able to definitively establish whether (3+1) models are a viable solution to explain the LSND signal.

## B. Combined NSBL+LSND analysis

The second analysis we perform is a combined NSBL+LSND analysis, with the purpose of obtaining the (3+1) allowed regions in parameter space, in both  $(\sin^2 2\theta_{\mu e}, \Delta m^2)$  and  $(p_{\text{LSND}}, \Delta m^2)$  space. A combined analysis of this sort assumes statistically compatible results. In Section III A, we have shown that the LSND and NSBL results are marginally compatible, for (3+1) models. In the following, we refer to the NSBL+LSND dataset as the short-baseline (SBL) dataset, and we construct the  $\chi^2$  function:

$$\chi_{\text{SBL}}^2 \equiv \chi_{\text{NSBL}}^2 + \chi_{\text{LSND}}^2 \quad (8)$$

where the two contributions  $\chi_{\text{NSBL}}^2$  and  $\chi_{\text{LSND}}^2$  are now simultaneously minimized with respect to the same set of three oscillation parameters  $\Delta m^2$ ,  $U_{e4}$ ,  $U_{\mu 4}$ . Figs. 4a and 4b show the 90%, 95%, and 99% CL 3-dimensional allowed regions in  $(\Delta m^2, U_{e4}, U_{\mu 4})$  projected onto the  $(\sin^2 2\theta_{\mu e}, \Delta m^2)$  and  $(p_{\text{LSND}}, \Delta m^2)$  2-dimensional regions, respectively, from the combined (3+1) analysis of SBL data. In this combined analysis, we use the same Monte Carlo method described in Section III A. We define the allowed regions in parameter space by performing a global scan. For example, the 95% CL allowed region in the three-dimensional space  $(\Delta m^2, U_{e4}, U_{\mu 4})$  is obtained by requiring  $\chi_{\text{SBL}}^2 - (\chi_{\text{SBL}}^2)_{\text{min}} < 7.82$ , where  $(\chi_{\text{SBL}}^2)_{\text{min}}$  is the global minimum  $\chi^2$  value. Fig. 4c shows the minimum  $\chi_{\text{SBL}}^2$  values obtained in the combined fit, as a func-

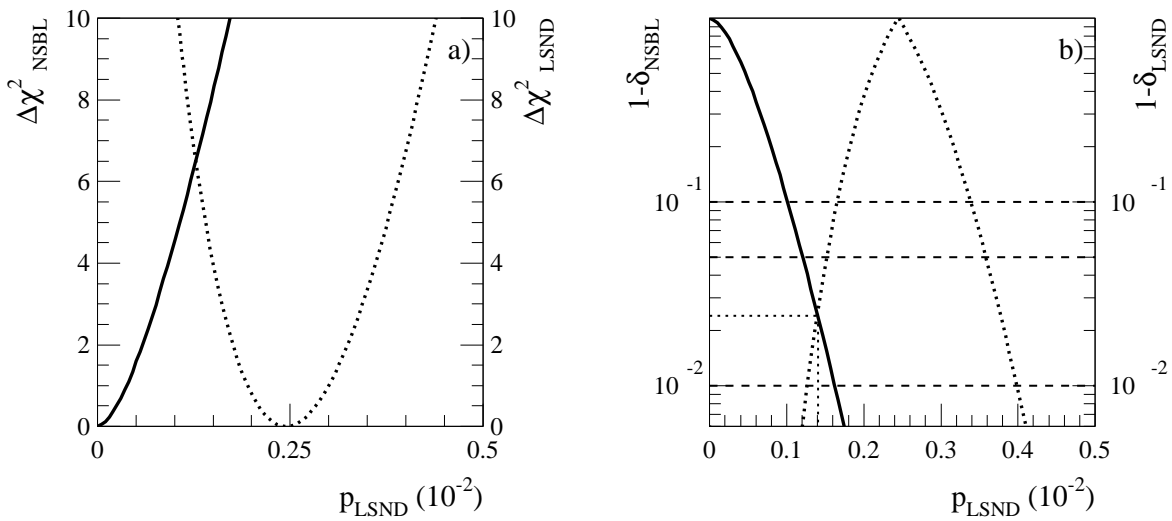


FIG. 3: a)  $\chi^2$  differences  $\Delta\chi^2_{\text{NSBL}}$ ,  $\Delta\chi^2_{\text{LSND}}$ , and b) individual confidence levels  $\delta_{\text{NSBL}}$ ,  $\delta_{\text{LSND}}$ , as a function of the LSND oscillation probability  $p_{\text{LSND}}$ , for the NSBL and LSND datasets. The curves are for (3+1) models with the neutrino mass splitting  $\Delta m^2$  fixed to the best-fit value  $\Delta m^2 = 0.92 \text{ eV}^2$  from the combined NSBL+LSND analysis, and variable mixing matrix elements  $U_{\mu 4}$ ,  $U_{e 4}$ . The solid curves refer to the NSBL dataset, the dotted ones to the LSND dataset. The dashed horizontal lines in Fig. 3b refer to the 90%, 95%, 99% individual confidence levels, the dotted horizontal line gives the combined confidence level  $\delta = \delta_{\text{NSBL}}(\delta_{\text{LSND}} + (1 - \delta_{\text{LSND}})/2)$  for which the NSBL and LSND datasets are incompatible.

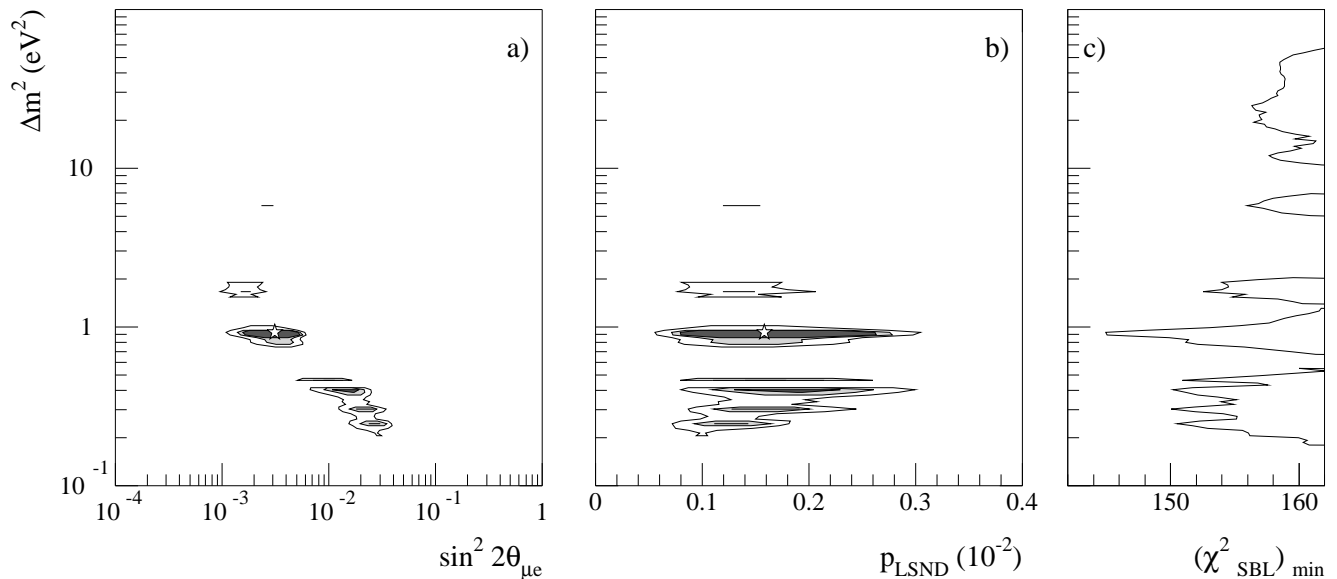


FIG. 4: Allowed regions in parameter space from a combined analysis of NSBL and LSND data, in (3+1) models, assuming statistical compatibility of the NSBL and LSND datasets. Fig. 4a shows the 90%, 95%, and 99% CL allowed regions in  $(\sin^2 2\theta_{\mu e}, \Delta m^2)$  space, together with the best-fit point, indicated by the star; b) shows the same allowed regions in  $(p_{\text{LSND}}, \Delta m^2)$  space; c) shows the minimum  $\chi^2$  value obtained in the combined analysis as a function of  $\Delta m^2$ . The number of degrees of freedom is 148.

tion of  $\Delta m^2$ . Of course, the  $\chi^2_{\text{SBL}}$  values shown in Fig. 4c for any given  $\Delta m^2$  value are larger than the sum of the two contributions  $\chi^2_{\text{NSBL}}$ ,  $\chi^2_{\text{LSND}}$ , shown in Figs. 2c,d for the same  $\Delta m^2$  value, since the latter were separately minimized with respect to the oscillation parameters. Similarly, Figs. 5a and 5b show the projections of the 90%,

95%, and 99% CL allowed regions in  $(\Delta m^2, U_{e 4}, U_{\mu 4})$  onto the  $(\sin^2 2\theta_{ee}, \Delta m^2)$  and  $(\sin^2 2\theta_{\mu\mu}, \Delta m^2)$  space, respectively, from the combined (3+1) analysis of SBL data. The zenith angle distribution of atmospheric muon neutrinos provides a constraint to  $\sin^2 \theta_{\mu\mu}$  that is not included in this SBL analysis; mixings to the right of the

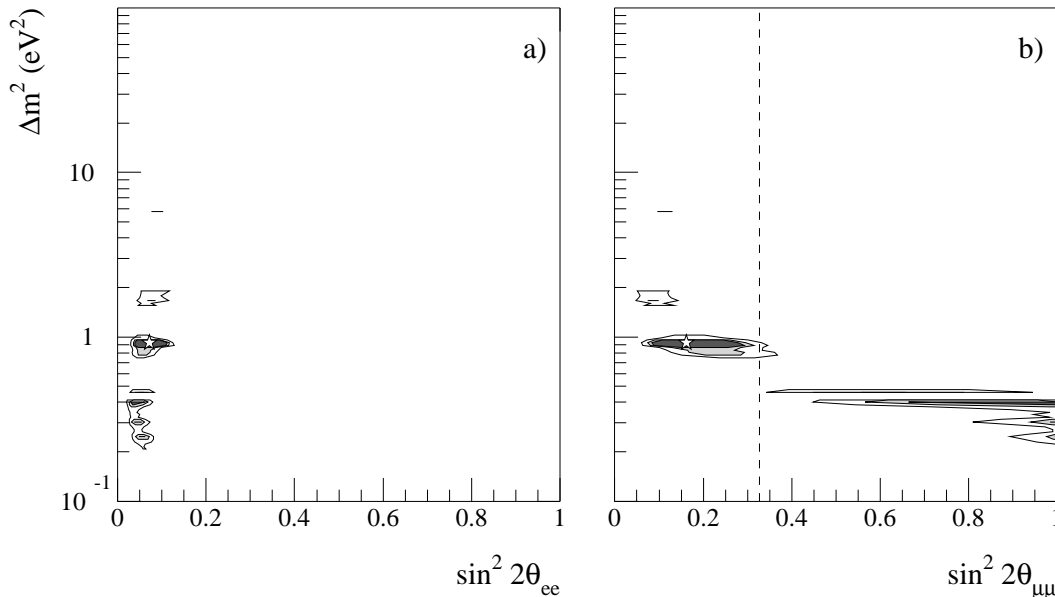


FIG. 5: Allowed regions in the parameter spaces relevant for  $\nu_e$  and  $\nu_\mu$  disappearance from a combined analysis of NSBL and LSND data, in (3+1) models, assuming statistical compatibility of the NSBL and LSND datasets. Fig. 5a shows the 90%, 95%, and 99% CL allowed regions in  $(\sin^2 2\theta_{ee}, \Delta m^2)$  space, together with the best-fit point, indicated by the star; b) shows the same allowed regions in  $(\sin^2 2\theta_{\mu\mu}, \Delta m^2)$  space. Mixings to the right of the dashed vertical line in Fig.5b are excluded at 90% CL by atmospheric neutrino results [34], which are not included in this analysis.

dashed vertical line in Fig.5b are excluded at 90% CL by atmospheric neutrino results [34]. The global  $\chi^2$  minimum is  $\chi^2_{\text{SBL}}=144.9$  (148 d.o.f.). This  $\chi^2$  value indicates an acceptable fit, assuming that the goodness-of-fit statistic follows the standard  $\chi^2$  p.d.f. [25]; for an alternative goodness-of-fit test, the reader should refer to Section V D. The individual NSBL and LSND contributions to the  $\chi^2$  minimum are  $\chi^2_{\text{NSBL}}=137.3$  and  $\chi^2_{\text{LSND}}=7.6$ , respectively. This best-fit point corresponds to the mass and mixing parameters  $\Delta m^2 = 0.92 \text{ eV}^2$ ,  $U_{e4} = 0.136$ ,  $U_{\mu 4} = 0.205$ .

#### IV. RESULTS FOR (3+2) MODELS

##### A. Statistical compatibility between NSBL and LSND

Having introduced the relevant oscillation probability formula in Eq. 5, and the statistical estimator  $p_{\text{LSND}}$  to compare the NSBL and LSND results in Section III A, we can now quantitatively address the statistical compatibility between the NSBL and LSND datasets under the (3+2) hypothesis.

Ideally, we would like to determine the NSBL upper limit for  $p_{\text{LSND}}$ , for all possible combinations of the mass parameters  $\Delta m^2_{41}$ ,  $\Delta m^2_{51}$ . This entails performing a scan equivalent to the one described in the (3+1) case as a function of  $\Delta m^2_{41}$ , shown in Fig. 2. In practice, the CPU-time requirements to pursue this route were

prohibitive.

An easier problem to tackle is to determine the statistical compatibility between the NSBL and LSND datasets only for the (3+2) models with mass splittings  $\Delta m^2_{41}$ ,  $\Delta m^2_{51}$  fixed to their best-fit values, as obtained by the combined NSBL+LSND analysis that we present in Section IV B. In sections III A and III B, we have demonstrated that, at least for (3+1) models, this choice is a good approximation for the best possible statistical compatibility (see Figs. 2 and 4).

In Fig. 6, we show the behavior of the  $\chi^2$  values  $\Delta\chi^2_{\text{NSBL}}$  and  $\Delta\chi^2_{\text{LSND}}$ , and of the confidence levels  $\delta_{\text{NSBL}}$  and  $\delta_{\text{LSND}}$ , as a function of  $p_{\text{LSND}}$ , for the set of (3+2) models satisfying the requirements  $\Delta m^2_{41} = 0.92 \text{ eV}^2$ ,  $\Delta m^2_{51} = 22 \text{ eV}^2$ . By analogy with Fig. 3, we map the four-dimensional space  $(U_{e4}, U_{\mu 4}, U_{e5}, U_{\mu 5})$  into the two-dimensional spaces  $(p_{\text{LSND}}, \chi^2_{\text{NSBL}})$  and  $(p_{\text{LSND}}, \chi^2_{\text{LSND}})$ , and we plot the minimum  $\chi^2$  values obtained for any given value of  $p_{\text{LSND}}$ . The confidence levels shown in Fig. 6b are obtained from Fig. 6a considering the four free parameters  $(U_{e4}, U_{\mu 4}, U_{e5}, U_{\mu 5})$  in the  $\chi^2_{\text{NSBL}}$  minimization process, and the two free parameters  $(U_{e4}U_{\mu 4}, U_{e5}U_{\mu 5})$  for  $\chi^2_{\text{LSND}}$ .

From Fig. 6b, we find that, in (3+2) models, the NSBL and LSND datasets are incompatible at an individual confidence level of  $\delta_{\text{NSBL}} = \delta_{\text{LSND}} = 1 - 0.215 = 78.5\%$ , and at a combined confidence level  $\delta = \delta_{\text{NSBL}}(\delta_{\text{LSND}} + (1 - \delta_{\text{LSND}})/2) = 70.0\%$ . Fig. 6 should be compared to Fig. 3, obtained for (3+1) models. A detailed comparison of the (3+1) and (3+2)

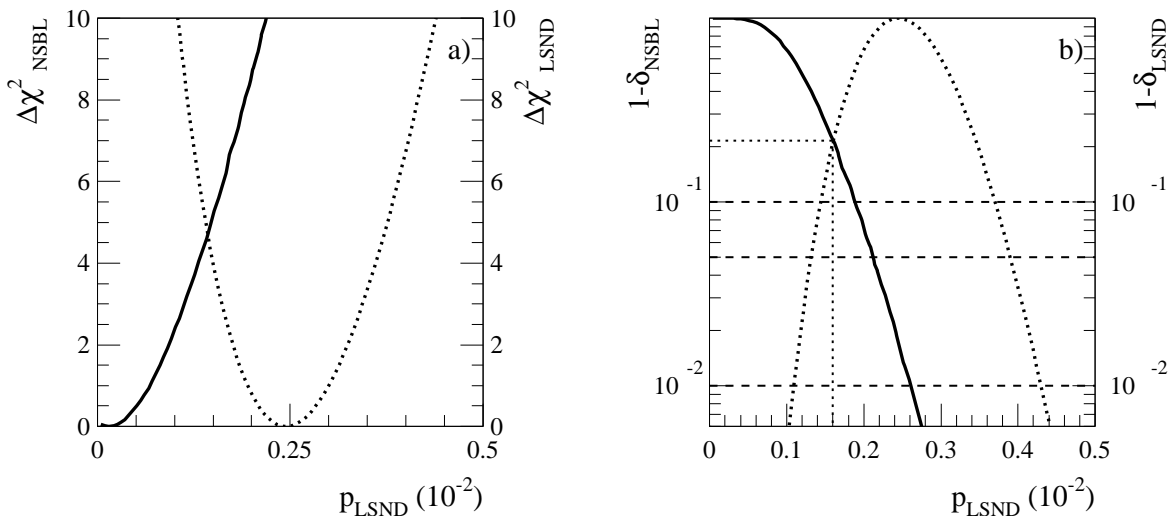


FIG. 6: a)  $\chi^2$  differences  $\Delta\chi^2_{\text{NSBL}}$  and  $\Delta\chi^2_{\text{LSND}}$ , and b) individual confidence levels  $\delta_{\text{NSBL}}$  and  $\delta_{\text{LSND}}$ , as a function of the LSND oscillation probability  $p_{\text{LSND}}$ , for the NSBL and LSND datasets. The curves are for (3+2) models with the neutrino mass splittings  $\Delta m_{41}^2$  and  $\Delta m_{51}^2$ , fixed to the best-fit values  $\Delta m_{41}^2 = 0.92 \text{ eV}^2$ ,  $\Delta m_{51}^2 = 22 \text{ eV}^2$  from the combined NSBL+LSND analysis, and variable mixing matrix elements  $U_{e4}$ ,  $U_{\mu 4}$ ,  $U_{e5}$ ,  $U_{\mu 5}$ . The solid curves refer to the NSBL dataset, the dotted ones to the LSND dataset. The dashed horizontal lines in Fig. 6b refer to the 90%, 95%, 99% individual confidence levels, the dotted horizontal line gives the combined confidence level  $\delta = \delta_{\text{NSBL}}\delta_{\text{LSND}}$  for which the NSBL and LSND datasets are incompatible.

hypotheses is presented in Section V.

### B. Combined NSBL+LSND analysis

We now turn to a combined analysis of the NSBL and LSND results in (3+2) models, assuming statistical compatibility between the two datasets. The purpose of this combined analysis is to obtain the allowed regions in the mass parameter space  $(\Delta m_{41}^2, \Delta m_{51}^2)$ , regardless of the simultaneous values for the mixing parameters. Results will be shown for  $\Delta m_{51}^2 \geq \Delta m_{41}^2$ ; the case  $\Delta m_{41}^2 > \Delta m_{51}^2$  can be obtained by simply interchanging  $\Delta m_{41}^2$  with  $\Delta m_{51}^2$ . The 95% CL allowed region is defined as the  $(\Delta m_{41}^2, \Delta m_{51}^2)$  for which  $\chi^2_{\text{SBL}} - (\chi^2_{\text{SBL}})_{\text{min}} < 5.99$ , where  $(\chi^2_{\text{SBL}})_{\text{min}}$  is the absolute  $\chi^2$  minimum for all  $(\Delta m_{41}^2, \Delta m_{51}^2)$  values. In the minimization procedure, the mixing matrix elements  $U_{e4}$ ,  $U_{\mu 4}$ ,  $U_{e5}$ ,  $U_{\mu 5}$ , are treated as free parameters. Fig. 7 shows the 90% and 99% CL allowed regions in  $(\Delta m_{41}^2, \Delta m_{51}^2)$  space obtained in the combined (3+2) analysis. In light of the (3+1) analysis shown in previous sections, the result is not surprising, pointing to favored masses in the range  $\Delta m_{41}^2 \simeq 0.9 \text{ eV}^2$ ,  $\Delta m_{51}^2 \simeq 10 - 40 \text{ eV}^2$ , at 90% CL. At 99% CL, the allowed region extends considerably, and many other  $(\Delta m_{41}^2, \Delta m_{51}^2)$  combinations appear. The best-fit model ( $\chi^2_{\text{SBL}}=135.9$ , 145 d.o.f.) is described by the following set of parameters:  $\Delta m_{41}^2 = 0.92 \text{ eV}^2$ ,  $U_{e4} = 0.121$ ,  $U_{\mu 4} = 0.204$ ,  $\Delta m_{51}^2 = 22 \text{ eV}^2$ ,  $U_{e5} = 0.036$ , and  $U_{\mu 5} = 0.224$ . We note here that the best-fit is not obtained for fourth and fifth mass eigenstates with de-

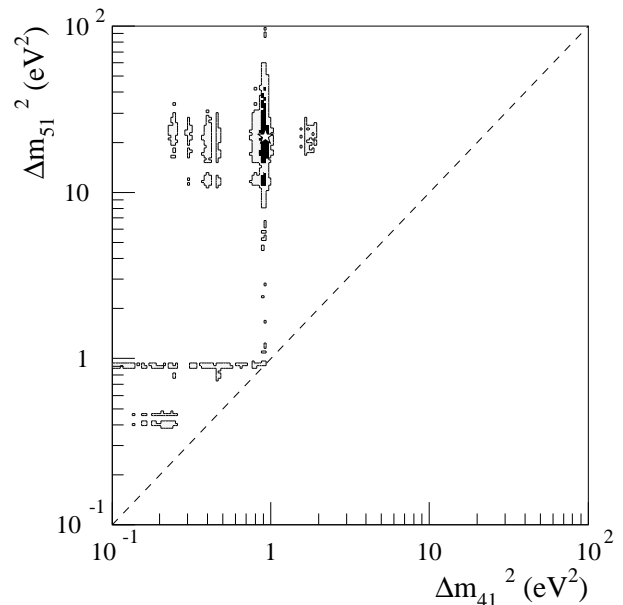


FIG. 7: Allowed ranges in  $(\Delta m_{41}^2, \Delta m_{51}^2)$  space for (3+2) models, for the combined NSBL+LSND analysis, assuming statistical compatibility between the NSBL and LSND datasets. The star indicates the best-fit point, the dark and light grey-shaded regions indicate the 90 and 99% CL allowed regions, respectively. Only the  $\Delta m_{51}^2 > \Delta m_{41}^2$  region is shown; the complementary region  $\Delta m_{41}^2 \geq \Delta m_{51}^2$  can be obtained by interchanging  $\Delta m_{41}^2$  with  $\Delta m_{51}^2$ .

generate masses, that is for  $\Delta m_{41}^2 \simeq \Delta m_{51}^2$ . The best-fit model we found for sub-eV neutrino masses is:  $\Delta m_{41}^2 =$



$0.46 \text{ eV}^2$ ,  $U_{e4} = 0.090$ ,  $U_{\mu4} = 0.226$ ,  $\Delta m_{51}^2 = 0.89 \text{ eV}^2$ ,  $U_{e5} = 0.125$ ,  $U_{\mu4} = 0.160$ , corresponding to  $\chi_{\text{SBL}}^2 = 141.5$  (145 d.o.f.).

## V. COMPARING THE (3+1) AND (3+2) FITS TO SBL DATA

In this section, we discuss four statistical tests that can be used to quantify the better overall agreement of SBL data to a (3+2) hypothesis for neutrino oscillations, compared to a (3+1) one.

### A. Test 1: NSBL upper limit on $p_{\text{LSND}}$ at a given confidence level $\delta_{\text{NSBL}}$

Test 1 uses only NSBL data to establish the (3+1) and (3+2) upper bounds on the LSND oscillation probability  $p_{\text{LSND}}$ . From Figs. 3 and 6, we obtain at a confidence level  $\delta_{\text{NSBL}} = 0.90$  (0.99):

$$(3+1): p_{\text{LSND}} < 0.100\% \text{ (0.162\%)}$$

$$(3+2): p_{\text{LSND}} < 0.186\% \text{ (0.262\%)}$$

Therefore, we find that (3+2) models can enhance the LSND probability  $p_{\text{LSND}}$  by quite a large factor, compared to (3+1) models. The increase in  $p_{\text{LSND}}$  that we obtain is significantly larger than the 25% increase found in [28], which is based on a specific choice of mixing parameters, as opposed to the complete parameter scan performed in this work. The value for the  $\bar{\nu}_\mu \rightarrow \bar{\nu}_e$  oscillation probability measured by LSND [6] is  $p_{\text{LSND}} = (0.264 \pm 0.067 \pm 0.045)\%$ , where the errors refer to the  $1\sigma$  statistical and systematic errors, respectively.

### B. Test 2: statistical compatibility between the NSBL and LSND datasets

Test 2 uses both the NSBL and LSND datasets, and treats them independently to find the combined confidence level  $\delta = \delta_{\text{NSBL}}(\delta_{\text{LSND}} + (1 - \delta_{\text{LSND}})/2)$  for which the datasets are incompatible, both in (3+1) and (3+2) models. The combined confidence levels can also be read from Figs. 3 and 6:

$$(3+1): \delta = 96.4\%$$

$$(3+2): \delta = 70.0\%$$

Therefore, we find that in (3+1) models the two datasets are marginally compatible, and the agreement is better in (3+2) models.

### C. Test 3: likelihood ratio test

Test 3 combines the NSBL and LSND datasets into a single, joint analysis. The likelihood ratio test [35] provides a standard way to assess whether two hypotheses can be distinguished in a statistically significant way. We define the maximum likelihood  $\mathcal{L}_i$  from the minimum  $\chi^2$  values  $(\chi_{\text{SBL}}^2)_{\text{min},i}$  as  $\mathcal{L}_i \equiv \exp(-(\chi_{\text{SBL}}^2)_{\text{min},i}/2)$ , where the index  $i = 1, 2$  refers to the (3+1) and (3+2) hypotheses, respectively. We can then form the likelihood ratio  $\lambda_{1,2} \equiv \mathcal{L}_1/\mathcal{L}_2$ . If the (3+1) hypothesis were as adequate as the (3+2) hypothesis in describing SBL data, the quantity

$$\chi_{1,2}^2(3) \equiv -2 \ln \lambda_{1,2} = (\chi_{\text{SBL}}^2)_{\text{min},1} - (\chi_{\text{SBL}}^2)_{\text{min},2} \quad (9)$$

should be distributed as a  $\chi^2$  distribution with three degrees of freedom, where the number of degrees of freedom is the difference in the number of mass and mixing parameters in the (3+2) and (3+1) hypotheses,  $6-3=3$ .

In our combined fits, we obtain (see Sections III B and IV B):

$$(3+1): (\chi_{\text{SBL}}^2)_{\text{min},1} = 144.9, \quad (148 \text{ d.o.f.})$$

$$(3+2): (\chi_{\text{SBL}}^2)_{\text{min},2} = 135.9, \quad (145 \text{ d.o.f.})$$

and therefore  $\chi_{1,2}^2(3) = 9.0$ . This value is significantly larger than 3: the probability for a  $\chi^2$  distribution with three degrees of freedom to exceed the value 9.0 is only 2.9%. In other words, according to the likelihood ratio test, the (3+1) hypothesis should be rejected compared to the (3+2) one at the 97.1% CL. Therefore, based on this test, we conclude from test 3 also that (3+2) models fit SBL data significantly better than (3+1) models.

### D. Test 4: compatibility using the “parameter goodness-of-fit”

Test 4 uses both the results of the individual NSBL and LSND analyses, as well as the results of the combined NSBL+LSND analysis. The test is based on the “parameter goodness-of-fit” [36] to compare the compatibility of the NSBL and LSND results under the (3+1) and (3+2) hypotheses. The test avoids the problem that a possible disagreement between the two results is diluted by data points which are insensitive to the mass and mixing parameters that are common to both datasets. The number of parameters common to both datasets is  $P_c = 2$  in (3+1) models, and  $P_c = 4$  in (3+2) models. One possible choice of common parameters is  $(\Delta m_{41}^2, U_{e4}U_{\mu4})$  for (3+1) models,  $(\Delta m_{41}^2, U_{e4}U_{\mu4}, \Delta m_{51}^2, U_{e5}U_{\mu5})$  for (3+2) models. The test is based on the statistic  $\chi_{\text{PG}}^2 = \chi_{\text{PG,NSBL}}^2 + \chi_{\text{PG,LSND}}^2$ , where  $\chi_{\text{PG,NSBL}}^2 \equiv (\chi_{\text{NSBL}}^2)_{\text{SBL min}} - (\chi_{\text{NSBL}}^2)_{\text{NSBL min}}$  and  $\chi_{\text{PG,LSND}}^2 \equiv (\chi_{\text{LSND}}^2)_{\text{SBL min}} - (\chi_{\text{LSND}}^2)_{\text{LSND min}}$  are the (positive) differences for the NSBL and LSND  $\chi^2$  values obtained by minimizing the entire SBL  $\chi^2$  function, minus the  $\chi^2$  values that best fit the individual datasets.

Model	$\chi_{\text{PG,NSBL}}^2$	$\chi_{\text{PG,LSND}}^2$	$\chi_{\text{PG}}^2$	$P_c$	PG (%)
(3+1)	11.8	4.3	16.1	2	$3.2 \cdot 10^{-2}$
(3+2)	7.1	4.4	11.5	4	2.1

TABLE I: Parameter goodness-of-fit PG, as defined in [36], to test the statistical compatibility between the NSBL and LSND datasets under the (3+1) and (3+2) hypotheses. The quantities  $\chi_{\text{PG,NSBL}}^2$  and  $\chi_{\text{PG,LSND}}^2$  are the NSBL and LSND contributions to the test statistic  $\chi_{\text{PG}}^2$  defined in the text;  $P_c$  indicates the number of parameters common to both datasets.

Table I gives the values for the parameter goodness-of-fit PG as defined in [36], based on the  $\chi_{\text{PG}}^2$  statistic, and the number of parameters common to the NSBL and LSND datasets,  $P_c$ . This test shows a dramatic improvement in the compatibility between the NSBL and LSND results in going from a (3+1) to a (3+2) model, raising the compatibility by nearly two orders of magnitude, from 0.03% to 2.1%. It will be interesting to investigate if (3+3) models can improve the compatibility further. The resulting compatibility levels obtained with the parameter goodness-of-fit method are lower than those found in Section VB; this, however, is not surprising, since the two statistical tests are quite different.

## VI. ADDITIONAL CONSTRAINTS

The (3+1) and (3+2) models discussed in this work should be confronted with additional experimental constraints, other than the ones discussed in detail in the previous sections. We limit ourselves here to list and comment on some of these constraints, rather than address them in a quantitative way. Mostly, we will discuss the impact that such additional constraints may have on the best-fit (3+1) and (3+2) models found in Sections III and IV.

First, nonzero mixing matrix elements  $U_{e4}$ ,  $U_{\mu4}$ ,  $U_{e5}$ , and  $U_{\mu5}$  may cause observable effects in atmospheric neutrino data, in the form of zenith angle-independent suppressions of the  $\nu_\mu$  and  $\nu_e$  survival probabilities. Since our analysis of SBL data tends to give larger values for muon, rather than electron, flavor content in the fourth and fifth mass eigenstate, the effect should be larger on muon atmospheric neutrinos. For example, the (3+1) and (3+2) best-fit models from Sections III B and IV B would give an overall suppression of the  $\nu_\mu$  flux of 8% and 17%, respectively. The size of the effect of  $\nu_\mu \rightarrow \nu_x$  oscillations at high  $\Delta m^2$  is comparable to the current accuracy with which the absolute normalization of the atmospheric neutrino flux is known [37], which is approximately 20%. A more quantitative analysis using the full Super-Kamiokande and MACRO spectral information [34] puts an upper bound of 16% at 90% CL on this high  $\Delta m^2$  contribution to the atmospheric  $\nu_\mu$  flux suppression (in the notation of Ref. [34], this suppres-

sion is parametrized as  $2d_\mu(1 - d_\mu)$ , where  $d_\mu < 0.09$  at 90% CL). Therefore, it is expected that the inclusion of atmospheric neutrino data in this analysis would pull the best-fit muon flavor components in the fourth and fifth mass eigenstates to lower values, but not in a dramatic way (see also Fig. 5b).

Second, models with large masses  $m_4$  and  $m_5$ , and with nonzero mixing matrix elements  $U_{e4}$  and  $U_{e5}$ , should be confronted with tritium  $\beta$  decay measurements. The presence of neutrino masses  $m_4$  and  $m_5$  introduces kinks in the differential  $\beta$  spectrum; the location in energy of the kinks is determined by the neutrino masses, and the size of the kinks is determined by the amount of electron flavor component in the fourth and fifth mass eigenstates. For a spectrometer integrating over the electron energy interval  $\delta$  near the  $\beta$ -decay endpoint, the count rate is [38]:

$$n(\delta) = \frac{\bar{R}}{3} \sum_{i=1}^n U_{ei}^2 (\delta^2 - m_i^2)^{3/2} \quad (10)$$

where the quantity  $\bar{R}$  does not depend on the small neutrino masses and mixings,  $n = 4$  or  $n = 5$  for (3+1) or (3+2) models, respectively, and we have assumed  $\delta > m_i$ ,  $i = 1, \dots, n$ , and CP invariance. From the experimental point of view, tritium  $\beta$  decay results are generally expressed in terms of a single effective mass  $m(\nu_e)$ :

$$n_s(\delta) = \frac{\bar{R}}{3} (\delta^2 - m(\nu_e)^2)^{3/2} \quad (11)$$

where  $m(\nu_e)$  is the fit mass parameter. In the limit  $\delta^2 \gg m_i^2$ ,  $i = 1, \dots, n$  the relation between the true masses and mixings to the fitted mass  $m(\nu_e)$  is independent from the integration interval  $\delta$ :

$$m(\nu_e)^2 \simeq \sum_{i=1}^n U_{ei}^2 m_i^2 \quad (12)$$

The condition  $\delta^2 \gg m_i^2$ ,  $i = 1, \dots, n$  is generally satisfied for the neutrino masses considered in this paper, in order to ensure sufficient  $\beta$  decay count rate statistics in the experiments. Therefore, to a first approximation, we can consider the effect of heavy neutrino masses  $m_4$ ,  $m_5$  only on the single mass parameter  $m(\nu_e)$  fitted by the experiments. A more general analysis assessing the sensitivity of current and future  $\beta$  decay experiments to multiple fitted neutrino masses, although highly desirable, is beyond the scope of this work; for further details, the reader should consult Ref. [38]. The current best measurements on  $m(\nu_e)^2$  come from the Troitsk and Mainz experiments [39], which have very similar  $m(\nu_e)^2$  sensitivities. Both found no evidence for a nonzero  $m(\nu_e)^2$  value; the latest Mainz result is  $m(\nu_e)^2 = -1.6 \pm 2.5 \pm 2.1 \text{ eV}^2$ , or  $m(\nu_e) \leq 2.2 \text{ eV}$  at 95% CL, using  $\delta = 70 \text{ eV}$  [39]. Now, assuming a normal hierarchy ( $m_1 < m_4 < m_5$ ) with  $m_1 \simeq 0$ , the  $\beta$  decay neutrino mass in Eq. 12 can be

written as  $m(\nu_e) \simeq U_{e4}^2 \Delta m_{41}^2 + U_{e5}^2 \Delta m_{51}^2$ ; the best-fit (3+1) and (3+2) models found in this analysis would give  $m(\nu_e)^2 = 0.017 \text{ eV}^2$  and  $m(\nu_e)^2 = 0.042 \text{ eV}^2$ , respectively, that is  $m(\nu_e)$  values well below the current experimental sensitivity. The planned tritium  $\beta$  decay experiment KATRIN should be able to improve the sensitivity to  $m(\nu_e)$  by roughly an order of magnitude in the forthcoming years, thanks to its better statistics, energy resolution, and background rejection [40]. Specifically, the systematic and statistical (for  $\delta \gtrsim 30 \text{ eV}$ ) uncertainties on the single fitted mass  $m(\nu_e)^2$  quoted for KATRIN are 0.018 and 0.016  $\text{eV}^2$ , respectively [40], which should provide some sensitivity to the preferred (3+1) and (3+2) neutrino models with a normal mass hierarchy,  $m_1 < m_4 < m_5$ . We now consider mass spectra with an inverted hierarchy, defined here as  $m_4 < m_1$  for (3+1) models, and  $m_5 < m_4 < m_1$  for (3+2) models. We note that for (3+2) models other hierarchies are also possible, but those do not satisfy the implicit assumption  $|\Delta m_{51}^2| = |\Delta m_{54}^2| + |\Delta m_{41}^2|$  taken in this analysis. The  $\beta$  decay neutrino mass in Eq. 12 can now be written as  $m(\nu_e)^2 \simeq |\Delta m_{41}^2|$  for inverted (3+1) models, and as  $m(\nu_e)^2 \simeq |\Delta m_{51}^2|$  for inverted (3+2) models. Clearly, in this case the  $\beta$  decay constraints depend strongly on the values of  $|\Delta m_{41}^2|$ ,  $|\Delta m_{51}^2|$ , and models with  $\gtrsim 5 \text{ eV}^2$  mass splittings are already severely disfavored.

Third, introducing sterile neutrinos may affect a number of cosmological predictions, which are derived from various measurements [41]. The standard cosmological model predicts that sterile neutrinos in the  $\sim 1 \text{ eV}$  mass range with a significant mixing with active neutrinos would be present in the early Universe with the same abundance as the active neutrino species, in disagreement with cosmological observations [42, 43]. On the other hand, several models have been proposed that would reconcile sterile neutrinos with cosmological observations, for example suppressing thermal abundances for sterile neutrinos (see, *e.g.*, Ref.[42] and references therein). In particular, active-sterile oscillations in the early Universe may provide a natural mechanism to suppress the relic abundances of sterile neutrinos [44], and scenarios invoking multiple sterile neutrinos are being investigated [43].

## VII. CONCLUSIONS

We have performed a combined analysis of seven short-baseline experiments (Bugey, CHOOZ, CCFR84, CDHS, KARMEN, LSND, NOMAD) for both the (3+1) and the (3+2) neutrino oscillation hypotheses, involving one and two sterile neutrinos at high  $\Delta m^2$ , respectively. The motivation for considering more than one sterile neutrino arises from the tension in trying to reconcile, in a CPT-conserving, four-neutrino picture, the LSND signal for oscillations with the null results obtained by the other short-baseline experiments. Multiple (*e.g.* three) sterile neutrinos can also be motivated on theoretical grounds.

We have described two types of analyses for both the

(3+1) and (3+2) neutrino oscillation hypotheses. In the first analysis, we treat the LSND and the null short-baseline (NSBL) datasets separately, and we determine the statistical compatibility between the two. In the second analysis, we assume statistical compatibility and we combine the two datasets, to obtain the favored regions in neutrino mass and mixing parameter space.

The main results of the analysis are summarized in Section V, where we compare the adequacy of the (3+1) and (3+2) hypotheses in describing neutrino short-baseline data, by means of four statistical tests. First, we treat the LSND oscillation probability as a parameter that can be measured with NSBL data alone, and find that the NSBL 90% CL upper limit on the LSND oscillation probability can be significantly relaxed by going from (3+1) to (3+2) models, by about 80%. Second, the combined confidence level for which the NSBL and LSND datasets are incompatible is determined to be 96.4% and 70.0% in the analysis, for the (3+1) and (3+2) hypotheses, respectively. Third, a likelihood ratio test of the two hypotheses is discussed, and shows that the (3+1) hypothesis should be rejected compared to the (3+2) one at the 97.1% CL. Fourth, the parameter “goodness-of-fit” defined in [36] shows much better agreement between the NSBL and LSND results for (3+2) models than for (3+1) models.

In conclusion, we find that (3+1) models are only marginally allowed when considering all of the seven short-baseline results, including LSND, in agreement with previous analyses [28, 29, 30], and that (3+2) models can provide a better description of the data. Only the simplest neutrino mass and mixing patterns have been fully characterized in the literature so far, and the analysis described in this paper may be viewed as a simple attempt to explore more generic scenarios, which appear both experimentally and theoretically plausible. Given the bright potential for precision measurements by neutrino oscillation experiments in the near future, a more general phenomenological approach may be needed.

## Acknowledgments

We thank J. Bouchez, L. Camilleri, K. Eitel, J.J. Gomez-Cadenas, E. A. Hawker, G. B. Mills, E. Nagy, V. Valuev, and G. P. Zeller for kindly providing data used in this analysis. We thank K. N. Abazajian, G. Barenboim, S. J. Brice, K. Eitel, B. Kayser, W. C. Louis, M. Maltoni, J. Monroe, P. Nienaber, T. Schwetz, A. Y. Smirnov, and K. Whisnant for valuable discussions and useful suggestions. This work was supported by NSF.

## APPENDIX A: PHYSICS AND STATISTICAL ASSUMPTIONS

In this section, we briefly describe the physics and statistical assumptions used to obtain the approximate char-

acterizations of the short-baseline experiments used in the analysis. For the analysis of the Bugey, CDHS, and KARMEN data, we also refer to the excellent reference [30], which we followed closely.

The Bugey experiment [18] is sensitive to  $\bar{\nu}_e$  disappearance by measuring the charged-current interaction of  $\bar{\nu}_e$ 's produced by two nuclear reactors at the Bugey nuclear power plant. Two liquid scintillator detectors, located at different positions, are used. The signature for an antineutrino interaction is a positron and a delayed light pulse produced by the subsequent neutron capture on  ${}^6\text{Li}$ . Data are given for three baselines: 15, 40, and 95 m between neutrino production and detection. We follow the “normalized energy spectra” analysis discussed in the Bugey paper [18]. The data are presented as ratios of observed to predicted (for no oscillations) positron energy spectra, between 1 and 6 MeV positron energy. We use 25, 25, and 10 positron energy bins for the 15, 40, 95 m baselines, respectively. In the  $\chi^2$  analysis, fits included not only the mass and mixing parameters, but also five large scale deformations of the positron spectrum due to systematic effects. The experimental positron energy resolution and the neutrino baseline smearing are taken into account; the neutrino cross-section energy dependence within a positron energy bin is not (the energy bin widths are small).

Similarly, the CHOOZ experiment [21] investigates  $\bar{\nu}_e$  disappearance by observing interactions of  $\bar{\nu}_e$ 's produced by two nuclear reactors  $\simeq 1$  km away from the CHOOZ detector. The signature for a neutrino interaction is a delayed coincidence between the prompt  $e^+$  signal and the signal due to the neutron capture in the Gd-loaded scintillator. We follow “analysis A,” as discussed in the CHOOZ paper [21]. Data are given as positron yields as a function of energy. In this analysis, seven positron energy bins, between 0.8 and 6.4 MeV, are considered, for which the CHOOZ observations, as well as the predictions on the positron yields for the no-oscillation case from both reactors, are given in [21]. Because of the presence of two reactor sources, the  $\chi^2$  analysis comprises 14 positron yield bins for a given energy/baseline. We use the full covariance matrix to take into account the fact that the yields corresponding to the same energy bin are extracted for both reactors simultaneously, as is done in [21]. The analysis fits for the systematic uncertainty in the absolute normalization constant on the  $\bar{\nu}_e$  yield from the reactors, in addition to the mass and mixing parameters. Since we are interested in the  $\Delta m^2 > 0.1$  eV $^2$  range only, where no energy shape distortions are expected, we neglect the systematic uncertainty on the energy-scale calibration, and the effect of the positron energy resolution.

The CCFR84 experiment [19] constrains  $\nu_\mu$  and  $\bar{\nu}_\mu$  disappearance by measuring the charged-current interaction of muon neutrinos and antineutrinos, produced by a Fermilab secondary, sign selected beam yielding  $40 < E_\nu < 230$  GeV neutrinos from  $\pi^\pm$  and  $K^\pm$  decays in the 352 m long decay pipe. We refer here to

the 1984 CCFR experiment (hence the label CCFR84 throughout the text), which operated with two similar detectors located at different distances from the neutrino source, 715 and 1116 m from the mid-point of the decay region, respectively. The two sampling calorimeter detectors consisted of steel plates and scintillation counters. Six secondary beam momentum settings were used: five for neutrino running, and one for antineutrino running. For each secondary beam momentum setting, the data are divided into three neutrino energy bins, for a total of eighteen energy bins, from Ref.[45]. Data are presented as double ratios: the far to near detector ratio of observed number of events, divided by the far to near ratio of events predicted for no oscillations. As in [19], only the mean neutrino energy for a given neutrino energy bin is used in the  $\chi^2$  analysis. The systematic and statistical uncertainties on the far to near ratio normalization are taken into account. The systematic uncertainty is assumed to be energy-independent and totally correlated between any two energy bins. The neutrino pathlength smearing, mostly due to the long decay region, is also taken into account.

The CDHS experiment [20] is also sensitive to  $\nu_\mu$  disappearance via the charged-current interaction of  $\nu_\mu$ 's, produced by a 19.2 GeV/c proton beam from the CERN Proton Synchrotron. Two detectors are located at 130 and 835 m from the target. The detectors are sampling calorimeters, with iron and scintillator modules interspersed, to measure the range of a muon produced in a neutrino interaction. Fifteen muon range bins are used. The data are presented as double ratios: the far to near detector ratio of the observed number of events, divided by the far to near ratio of the number of events predicted for no oscillations. Neutrino energy distributions are obtained for a given muon energy (or range) via the NUANCE [46] neutrino cross-section generator. As for CCFR84, the systematic uncertainty on the far to near ratio and the neutrino baseline smearing are taken into account.

The KARMEN experiment [22] investigates the  $\bar{\nu}_\mu \rightarrow \bar{\nu}_e$  appearance channel, from  $\bar{\nu}_\mu$ 's produced in the  $\pi^+ \rightarrow \mu^+ + \bar{\nu}_\mu$  decay at rest (DAR) chain of the ISIS neutrino source. KARMEN measures the charged-current interaction  $p(\bar{\nu}_e, e^+)n$ , with a liquid scintillator detector located at an average distance 17.7 m downstream of the neutrino source. The  $\bar{\nu}_e$  signature is a spatially correlated delayed coincidence between a prompt positron and a delayed  $\gamma$  event from a  $(n, \gamma)$  neutron capture reaction. In this analysis, only the positron (“prompt”) energy distribution after all cuts is taken into account, given in [22]. The data are binned into nine prompt energy bins, between 16 and 50 MeV (all bins are 4 MeV wide, except the highest energy one, ranging from 48 to 50 MeV). In predicting the prompt energy distribution for a set of mass and mixing oscillation parameters, the given Monte Carlo positron energy distribution, and the total number of events expected after all cuts for full mixing and  $\Delta m^2 = 100$  eV $^2$ , are used [47]. Energy resolution and

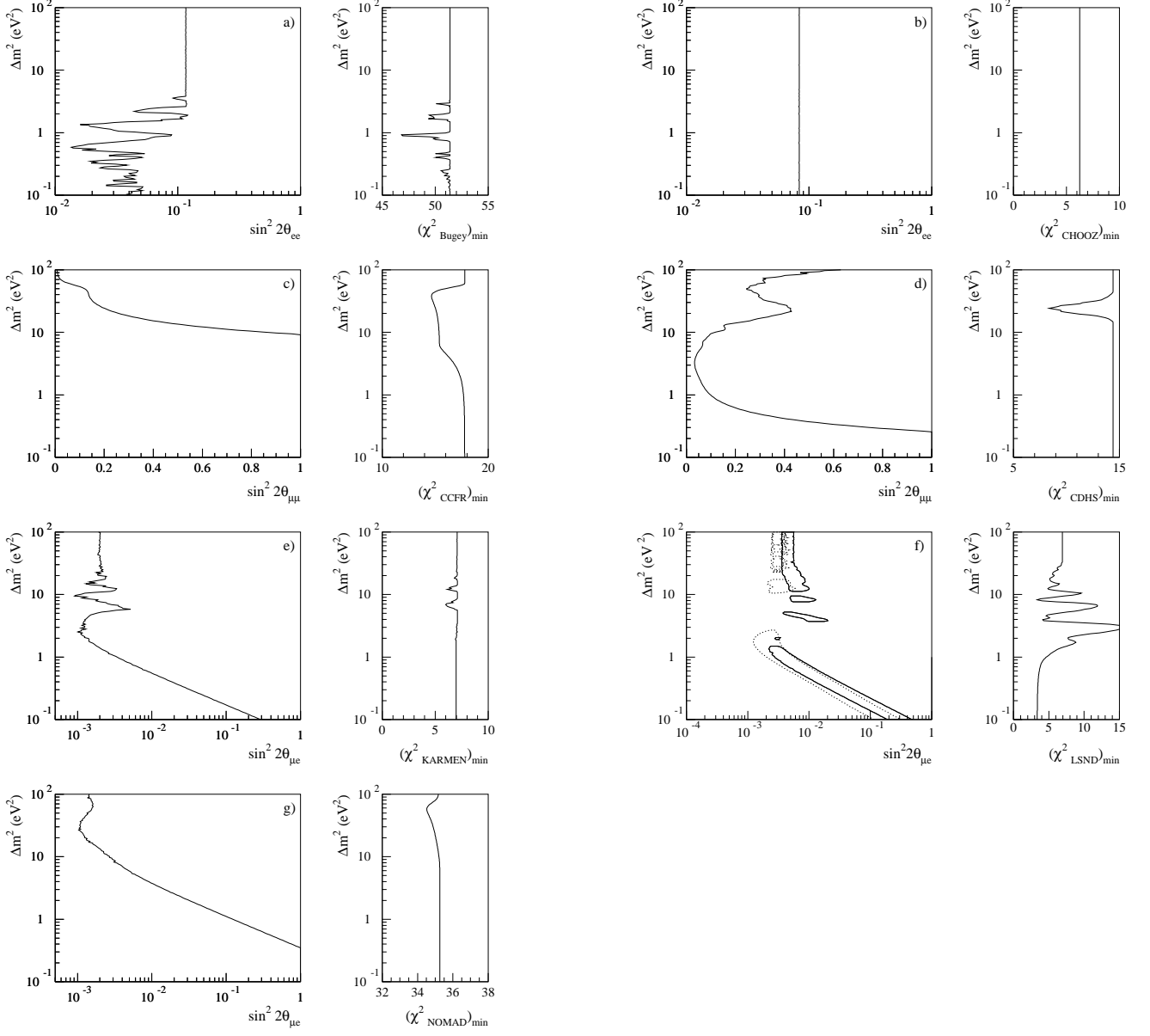


FIG. 8: 90% CL upper limits on oscillations derived in this analysis for the following NSBL experiments: a) Bugey, b) CHOOZ, c) CCFR84, d) CDHS, e) KARMEN, g) NOMAD. Fig. 8f shows the LSND 90% CL allowed region obtained with the decay-at-rest analysis described in Appendix A (solid line), superimposed to the published LSND 90% CL allowed region (dashed line). Also shown are the  $(\chi^2)_{\min}$  values as a function of  $\Delta m^2$  obtained by all the experiments considered individually. The number of degrees of freedom is 58 in Bugey, 12 in CHOOZ, 16 in CCFR84, 13 in CDHS, 7 in KARMEN, 3 in LSND, 28 in NOMAD.

baseline smearing effects (due to finite detector size) are taken into account. Given the low statistics of the nine KARMEN prompt energy bins, we construct the  $\chi^2$  function by first defining the likelihood ratio [25]:

$$\lambda(\theta) = \frac{f(\mathbf{n}; \mu(\theta), \mathbf{b})}{f(\mathbf{n}; \mathbf{n}, \mathbf{b})} \quad (\text{A1})$$

where  $\theta$  denotes schematically all mass and mixing parameters,  $\mathbf{n}$ ,  $\mu(\theta)$  and  $\mathbf{b}$  are the data, expected signal, and expected background vectors with nine elements, and  $f(\mathbf{n}; \mu(\theta), \mathbf{b})$  are the probabilities for a Poisson process

with known background:

$$f(\mathbf{n}; \mu(\theta), \mathbf{b}) = \prod_{i=1}^9 \frac{(\mu_i + b_i)^{n_i} \exp(-(\mu_i + b_i))}{n_i!} \quad (\text{A2})$$

We define  $\chi^2_{\text{KARMEN}}$  as:

$$\chi^2_{\text{KARMEN}} \equiv -2 \ln \lambda(\theta) \quad (\text{A3})$$

The LSND experiment at Los Alamos [6] is also sensitive to  $\bar{\nu}_\mu \rightarrow \bar{\nu}_e$  appearance, with a neutrino source

and detection signature similar to that of KARMEN, but with better statistics. The LSND liquid scintillator detector is located at an average distance of 30 m from the neutrino source. As for KARMEN, in this analysis we consider only the positron energy distribution arising from a  $\bar{\nu}_e$  interaction in mineral oil, published as five energy bins between 20 and 60 MeV [6]. Our analysis ignores the information arising from the higher-energy neutrinos from pions decaying in flight, which has a smaller (but non-negligible) sensitivity to oscillations compared to the decay at rest (DAR) sample considered here. In our simulation, we take into account the expected energy distribution from  $\mu^+$  decay at rest, the neutrino baseline distribution for the 8 m long cylindrical detector, the neutrino energy dependence of the cross-section for the detection process  $p(\bar{\nu}_e, e^+)n$  (including nuclear effects, simulated with the NUANCE [46] neutrino cross-section generator), and the experimental energy resolution. We use the published numbers for the background expectations, the number of  $\bar{\nu}_e$  events for 100%  $\bar{\nu}_\mu \rightarrow \bar{\nu}_e$  transmutation, and for the efficiency of the event selection criteria. We construct the LSND  $\chi^2$  function in the same way as we construct the one for KARMEN, because of the low statistics of the data sample.

Finally, the NOMAD experiment is sensitive to  $\nu_\mu \rightarrow \nu_e$  oscillations at  $\Delta m^2 \gtrsim 1 \text{ eV}^2$  by looking for charged-current muon neutrino and electron neutrino interactions in the NOMAD detector [23]. The detector consists of a large dipole magnet which houses drift chambers to measure the momenta of the charged particles produced in neutrino interactions; transition radiation modules for lepton identification; an electromagnetic calorimeter to measure the energy of electrons and photons; a hadron calorimeter for particle identification; and muon chambers for muon identification. Neutrinos are produced by impinging 450 GeV protons extracted from the CERN SPS accelerator onto a thick beryllium target. The secondary particles produced in the target are focused into a nearly parallel beam by two magnetic lenses, and decay in a 290 m long decay tunnel to produce a  $\sim 10 - 100 \text{ GeV}$  neutrino beam with about 1%  $\nu_e$  contamination. Neutrino interactions are then observed in the NOMAD detector at an average distance of 625 m from the neutrino source. The  $\nu_\mu \rightarrow \nu_e$  search is performed by comparing the measured ratio  $R_{e\mu}$  of the number of  $\nu_e$  to  $\nu_\mu$  charged-current neutrino interactions with the one expected in the absence of oscillations. The data are binned into 30 bins, covering ten bins in visible energy between 3 and 170 GeV, and three radial bins in the neutrino interaction vertex. A  $\chi^2$  analysis is performed, using the final NOMAD numbers on the observed and predicted electron-to-muon ratio, including statistical errors as well as the full error matrix describing systematic uncertainties and uncertainty correlations over different bins [48]. In predicting the effect of  $\nu_\mu \rightarrow \nu_e$  oscillations under any mass and mixing hypothesis, the contribution to  $R_{e\mu}$  from oscillations

with full mixing and  $\Delta m^2 = 5,000 \text{ eV}^2$  expected in NOMAD after all cuts is used [48]. Energy resolution and baseline smearing effects (due to the long decay region) are taken into account [23].

In Fig. 8, we show our calculations of the 90% CL upper limits on oscillations as a function of  $\Delta m^2$  for the six NSBL experiments considered here, as well as the 90% CL allowed region for LSND. The  $(\chi^2)_{\min}$  values as a function of  $\Delta m^2$  for all of the experiments are also shown. All the solid curves shown are obtained from the simplified analysis described here, and compare well with the published results [6, 18, 19, 20, 21, 22, 23].

The LSND region obtained in our analysis of DAR neutrinos is slightly shifted to the right compared to the final LSND area, shown in Fig. 8f as a dashed line, reflecting the difference in the two datasets. More detailed LSND DAR analyses give results in rough agreement with our allowed region [12, 26].

The  $(\chi^2)_{\min}$  values obtained for the Bugey and CDHS experiments as a function of  $\Delta m^2$  give details that might seem surprising, at first. Slightly better fits to the data are obtained under a neutrino oscillations hypothesis, as opposed to the no oscillations one. Therefore, we add a final comment to explain the results of these fits.

The Bugey fit is driven by the data at the shortest baseline, 15 m, where the statistical errors on the observed positron spectrum from  $\bar{\nu}_e$  interactions are the smallest. As explained in Ref.[18], systematic uncertainties are taken into account by allowing for linear deformations, as a function of positron energy, of the ratio of observed to predicted positron yields. The values of  $(\chi^2_{\text{Bugey}})_{\min}$  as a function of  $\Delta m^2$  are explained by the fact that, for certain  $\Delta m^2$  values, an oscillatory fit to the 15 m positron spectrum ratio describes the data marginally better than any straight line. Our best-fit oscillation hypothesis to Bugey data only is  $\Delta m^2 = 0.92 \text{ eV}^2$ ,  $\sin^2 2\theta_{ee} = 0.05$ .

For CDHS, the  $(\chi^2_{\text{CDHS}})_{\min}$  curve in Fig. 8d has a minimum at  $\Delta m^2 \simeq 20 - 30 \text{ eV}^2$ . This minimum is due to the fact that the far/near  $\nu_\mu$  rate ratio, corrected for the baseline and detector mass differences between the two detectors (as well as other minor effects), is measured to be slightly greater than one [20]:  $R_{\text{corr}} = 1.044 \pm 0.023 \pm 0.025$ . This marginal deviation from one causes the fit procedure to prefer more  $\nu_\mu$  disappearance by oscillations in the near than in the far detector. Given the average  $\nu_\mu$  energy (3.2 GeV) and pathlength (130 m) for neutrinos interacting in the CDHS near detector, this condition is satisfied in the  $\Delta m^2 = 20 - 30 \text{ eV}^2$  range. Our best-fit oscillation hypothesis to CDHS data only is  $\Delta m^2 = 24 \text{ eV}^2$ ,  $\sin^2 2\theta_{\mu\mu} = 0.29$ .

- 
- [1] Y. Fukuda *et al.* [Kamiokande Collaboration], Phys. Lett. B **335**, 237 (1994); R. Becker-Szendy *et al.*, Nucl. Phys. Proc. Suppl. **38**, 331 (1995); W. W. Allison *et al.* [Soudan-2 Collaboration], Phys. Lett. B **449**, 137 (1999). [arXiv:hep-ex/9901024].
- [2] Y. Fukuda *et al.* [Super-Kamiokande Collaboration], Phys. Rev. Lett. **81**, 1562 (1998) [arXiv:hep-ex/9807003].
- [3] M. Ambrosio *et al.* [MACRO Collaboration], Phys. Lett. B **517**, 59 (2001) [arXiv:hep-ex/0106049].
- [4] B. T. Cleveland *et al.*, Astrophys. J. **496**, 505 (1998); P. Anselmann *et al.* [GALLEX Collaboration], Phys. Lett. B **285**, 376 (1992). D. N. Abdurashitov *et al.*, Phys. Lett. B **328**, 234 (1994).
- [5] Q. R. Ahmad *et al.* [SNO Collaboration], Phys. Rev. Lett. **87**, 071301 (2001) [arXiv:nucl-ex/0106015]; Q. R. Ahmad *et al.* [SNO Collaboration], Phys. Rev. Lett. **89**, 011301 (2002) [arXiv:nucl-ex/0204008]; S. Fukuda *et al.* [Super-Kamiokande Collaboration], Phys. Lett. B **539**, 179 (2002) [arXiv:hep-ex/0205075].
- [6] C. Athanassopoulos *et al.* [LSND Collaboration], Phys. Rev. Lett. **77**, 3082 (1996) [arXiv:nucl-ex/9605003]; C. Athanassopoulos *et al.* [LSND Collaboration], Phys. Rev. C **58**, 2489 (1998) [arXiv:nucl-ex/9706006]; A. Aguilar *et al.* [LSND Collaboration], Phys. Rev. D **64**, 112007 (2001) [arXiv:hep-ex/0104049].
- [7] A. O. Bazarko [BooNe Collaboration], arXiv:hep-ex/9906003.
- [8] M. Maltoni, T. Schwetz and J. W. F. Valle, Phys. Rev. D **65**, 093004 (2002) [arXiv:hep-ph/0112103].
- [9] C. Giunti, M. C. Gonzalez-Garcia and C. Peña-Garay, Phys. Rev. D **62**, 013005 (2000) [arXiv:hep-ph/0001101].
- [10] G. Barenboim and F. Scheck, Phys. Lett. B **440**, 332 (1998) [arXiv:hep-ph/9808327]; G. Barenboim, A. Dighe and S. Skadhauge, Phys. Rev. D **65**, 053001 (2002) [arXiv:hep-ph/0106002].
- [11] H. Murayama and T. Yanagida, Phys. Lett. B **520**, 263 (2001) [arXiv:hep-ph/0010178]; G. Barenboim, L. Borisso, J. Lykken and A. Y. Smirnov, JHEP **0210**, 001 (2002) [arXiv:hep-ph/0108199]; G. Barenboim, L. Borisso and J. Lykken, arXiv:hep-ph/0212116.
- [12] M. Maltoni, T. Schwetz, M. A. Tortola and J. W. F. Valle, Nucl. Phys. B **643**, 321 (2002) [arXiv:hep-ph/0207157].
- [13] H. Paes, L. Song and T. J. Weiler, Phys. Rev. D **67**, 073019 (2003) [arXiv:hep-ph/0209373].
- [14] P. Ramond, arXiv:hep-ph/9809459.
- [15] R. N. Mohapatra and R. E. Marshak, Phys. Rev. Lett. **44**, 1316 (1980) [Erratum-ibid. **44**, 1643 (1980)].
- [16] R. R. Volkas, Prog. Part. Nucl. Phys. **48**, 161 (2002) [arXiv:hep-ph/0111326].
- [17] G. J. Stephenson, T. Goldman, B. H. J. McKellar and M. Garbutt, arXiv:hep-ph/0307245; K. S. Babu and G. Seidl, arXiv:hep-ph/0312285; K. L. McDonald, B. H. J. McKellar and A. Mastrano, arXiv:hep-ph/0401241.
- [18] Y. Declais *et al.*, Nucl. Phys. B **434**, 503 (1995).
- [19] I. E. Stockdale *et al.*, Phys. Rev. Lett. **52**, 1384 (1984).
- [20] F. Dydak *et al.*, Phys. Lett. B **134**, 281 (1984).
- [21] M. Apollonio *et al.*, arXiv:hep-ex/0301017.
- [22] B. Armbruster *et al.* [KARMEN Collaboration], Phys. Rev. D **65**, 112001 (2002) [arXiv:hep-ex/0203021].
- [23] P. Astier *et al.* [NOMAD Collaboration], Phys. Lett. B **570**, 19 (2003) [arXiv:hep-ex/0306037]; D. Gibin, Nucl. Phys. Proc. Suppl. **66**, 366 (1998); V. Valuev [NOMAD Collaboration], *Prepared for International Europhysics Conference on High-Energy Physics (HEP 2001), Budapest, Hungary, 12-18 Jul 2001*
- [24] B. Kayser, arXiv:hep-ph/0211134.
- [25] K. Hagiwara *et al.* [Particle Data Group Collaboration], Phys. Rev. D **66**, 010001 (2002).
- [26] E. D. Church, K. Eitel, G. B. Mills and M. Steidl, Phys. Rev. D **66**, 013001 (2002) [arXiv:hep-ex/0203023].
- [27] K. Eitel, New J. Phys. **2**, 1 (2000) [arXiv:hep-ex/9909036].
- [28] O. L. G. Peres and A. Y. Smirnov, Nucl. Phys. B **599**, 3 (2001) [arXiv:hep-ph/0011054].
- [29] A. Strumia, Phys. Lett. B **539**, 91 (2002) [arXiv:hep-ph/0201134].
- [30] W. Grimus and T. Schwetz, Eur. Phys. J. C **20**, 1 (2001) [arXiv:hep-ph/0102252].
- [31] F. James and M. Roos, Comput. Phys. Commun. **10**, 343 (1975).
- [32] G. J. Feldman and R. D. Cousins, Phys. Rev. D **57**, 3873 (1998) [arXiv:physics/9711021].
- [33] S. M. Bilenky, C. Giunti, W. Grimus and T. Schwetz, Phys. Rev. D **60**, 073007 (1999) [arXiv:hep-ph/9903454].
- [34] M. Maltoni, T. Schwetz and J. W. F. Valle, Phys. Lett. B **518**, 252 (2001) [arXiv:hep-ph/0107150].
- [35] W. T. Eadie, D. Drijard, F. E. James, M. Roos, B. Sadoulet, "Statistical Methods in Experimental Physics" (North Holland, Amsterdam, 1971).
- [36] M. Maltoni and T. Schwetz, Phys. Rev. D **68**, 033020 (2003) [arXiv:hep-ph/0304176]; M. Maltoni, T. Schwetz, M. A. Tortola and J. W. F. Valle, arXiv:hep-ph/0305312.
- [37] M. Honda, T. Kajita, K. Kasahara and S. Midorikawa, Phys. Rev. D **52**, 4985 (1995) [arXiv:hep-ph/9503439]; Y. Liu, L. Derome and M. Buenerd, Phys. Rev. D **67**, 073022 (2003) [arXiv:astro-ph/0211632].
- [38] Y. Farzan and A. Y. Smirnov, Phys. Lett. B **557**, 224 (2003) [arXiv:hep-ph/0211341]; Y. Farzan, O. L. G. Peres and A. Y. Smirnov, Nucl. Phys. B **612**, 59 (2001) [arXiv:hep-ph/0105105].
- [39] V. M. Lobashev *et al.*, Nucl. Phys. Proc. Suppl. **91**, 280 (2001); J. Bonn *et al.*, Nucl. Phys. Proc. Suppl. **91**, 273 (2001).
- [40] A. Osipowicz *et al.* [KATRIN Collaboration], arXiv:hep-ex/0109033; L. Bornschein [KATRIN Collaboration], eConf **C030626**, FRAP14 (2003) [arXiv:hep-ex/0309007].
- [41] D. N. Spergel *et al.*, arXiv:astro-ph/0302209; W. J. Percival *et al.*, arXiv:astro-ph/0105252. J. M. O'Meara, D. Tytler, D. Kirkman, N. Suzuki, J. X. Prochaska, D. Lubin and A. M. Wolfe, Astrophys. J. **552**, 718 (2001) [arXiv:astro-ph/0011179]; W. L. Freedman *et al.*, Astrophys. J. **553**, 47 (2001) [arXiv:astro-ph/0012376].
- [42] K. N. Abazajian, Astropart. Phys. **19**, 303 (2003) [arXiv:astro-ph/0205238].
- [43] P. Di Bari, arXiv:astro-ph/0302433; P. Di Bari, Phys. Rev. D **65**, 043509 (2002) [arXiv:hep-ph/0108182].
- [44] R. Foot, M. J. Thomson and R. R. Volkas, Phys. Rev. D **53**, 5349 (1996) [arXiv:hep-ph/9509327].
- [45] I. E. Stockdale, FERMILAB-THESIS-1984-08.

- [46] D. Casper, Nucl. Phys. Proc. Suppl. **112**, 161 (2002) [arXiv:hep-ph/0208030].
- [47] K. Eitel *et al.* [KARMEN collaboration], Nucl. Phys. Proc. Suppl. **77**, 212 (1999) [arXiv:hep-ex/9809007].
- [48] V. Valuev, private communication.